Viscous-inviscid interaction method for steady transonic flow

Article *in* Transactions of FAMENA · January 2011

CITATIONS
0

READS
22

2 authors:

Frane Majić
University of Zagreb
2 PUBLICATIONS **1** CITATION
SEE PROFILE

Zdravko Virag
University of Zagreb
34 PUBLICATIONS **74** CITATIONS
SEE PROFILE

Frane Majić
Zdravko Virag

ISSN 1333-1124

VISCOUS-INVISCID INTERACTION METHOD FOR STEADY TRANSONIC FLOW

UDC 532.511:532.517.2

Summary

A numerical method for steady load determination on airfoils in a transonic flow with the occurrence of a shock wave is demonstrated. The method implements the Euler equations for the inviscid region and integral boundary layer equations for the viscous region near an airfoil. The viscous-inviscid interaction is implemented through transpiration velocity. The Euler solution is calculated by applying the Van Leer flux-vector splitting on a body-fitted C-grid. The boundary layer model is calculated applying Drela's model of integral boundary layer equations for a laminar and a turbulent flow. The transition is predicted by the e^n method. The viscous-inviscid interaction method is carried out in a direct mode. The method gave comparable results with the calculated RANS results and experimental data, while time and computational costs were slightly higher than for the pure Euler calculations. The method predicted the position of a shock wave slightly shifted toward the trailing edge of airfoil with respect to the position obtained by experiment, but in front of the RANS and Euler results.

Key words: *viscous-inviscid coupling, transonic flow, airfoil, transpiration velocity*

1. Introduction

Optimization in the transonic airfoil design still requires computationally efficient methods for the determination of airfoil aerodynamic loads. As considerable effort is needed for computing aerodynamic loads, more efficient methods have been developed for the task of their predicting. Since the simulation of a transonic flow around an airfoil adopts the most precise modelling techniques like RANS (Reynolds Averaged Navier-Stokes), DES (Detached Eddy Simulation) or LES (Large Eddy Simulation), it requires extremely high computational effort. This stems from the fact that in a steady transonic flow one has to take into account three parameters, namely the Reynolds number, the Mach number and the angle of attack. With a combination of these three parameters, the number of required aerodynamic simulations which fall into flight envelope grows very fast. For this purpose, panel methods are still present in the actual design analysis because of low computer time consumption and a simple setting procedure of computational problem. One of the method drawbacks is the inability of capturing strong shock waves in transonic flows. Recently, Leifsson and Koziel [1] have employed the transonic small disturbance (TSD) method for the analysis of aerodynamic loads in the optimization process of transonic airfoil. Also, Hacioglu and Özkol

[2] used a full potential flow-field solver in a transonic case for the inverse design and airfoil optimization problem which was coupled with a vibrational genetic algorithm. The RANS simulation gives much more accurate results, but it uses a large amount of computational time. In addition, it needs large grids with high resolution and the problem setting is much more demanding. Therefore, DES and LES are certainly out of scope for such applications. Between these extremes, viscous-inviscid interaction methods are a good compromise. In one family of these methods, the inviscid region is solved by the panel method or the TSD method and the viscous thin region near an airfoil is solved by the boundary layer model. The other family employs a Euler solver for the inviscid part and a boundary layer model for the viscous part of flow. The Euler solver is capable of resolving strong shocks and with the boundary layer coupling it is a good balance between a flow model and computational efficiency.

In this article, a coupled method of the Euler and integral boundary layer equations is developed. A boundary layer model is described with integral equations and coupled with the steady Euler equations through transpiration velocity. The steady Euler solution is calculated applying the Van Leer flux-vector splitting method in generalized coordinates, and the theory of characteristics is used for the development of boundary conditions at the outer boundary. The boundary condition is applied explicitly to the airfoil contour. The developed viscous-inviscid interaction method gives results comparable to RANS solvers, but the computational time is several times shorter and this is a significant advantage for the fast airfoil optimization analysis in the design process. The method is able to capture strong shocks and viscous effects.

2. Numerical method

2.1. Inviscid model

The inviscid model employs the two-dimensional Euler equations for an ideal gas. The equations are transformed to a moving body-fitted coordinate system (ξ,η,τ) and are given in a conservative form by

$$\frac{\partial \hat{Q}}{\partial \tau}+\frac{\partial \hat{F}}{\partial \xi}+\frac{\partial \hat{G}}{\partial \eta}=0, \tag{1}$$

where

$$\hat{Q}=JQ, \tag{2}$$

$$\hat{F}=(-y_\eta x_\tau + x_\eta y_\tau)Q + y_\eta F - x_\eta G, \tag{3}$$

$$\hat{G}=(-x_\xi y_\tau + y_\xi x_\tau)Q - y_\xi F - x_\xi G. \tag{4}$$

Vectors Q, F and G represent the vectors of conservative variables, the fluxes in the Cartesian x- and y-coordinates, respectively:

$$Q=\begin{bmatrix}\rho\\ \rho u\\ \rho v\\ \rho e\end{bmatrix}, \quad F=\begin{bmatrix}\rho u\\ \rho u^2+p\\ \rho uv\\ \rho uh\end{bmatrix}, \quad G=\begin{bmatrix}\rho v\\ \rho vu\\ \rho v^2+p\\ \rho vh\end{bmatrix}. \tag{5}$$

In the vectors defined by expressions (5), ρ is the fluid density, p is pressure, u and v are the Cartesian x and y velocity components respectively, e is the specific total energy, and

h is the specific total enthalpy. ξ and η are the spatial body-fitted coordinates and τ is the time coordinate which is equal to the physical time. In equations (2), (3), (4) and in the equations below the subscripts ξ, η, and τ represent the derivatives of the physical coordinates with respect to the body-fitted coordinates. J is the Jacobian of the transformation and is equal to $J = x_\xi y_\eta - y_\xi x_\eta$. The inviscid model employs the flux vector splitting schemes devised by Van Leer [3]. Correct splitting of transformed flux vectors is made by rewriting $\hat{F}$ and $\hat{G}$ as the product of a local rotation matrix (T_F and T_G) and the modified flux vector, which has the same form as the Cartesian flux vector but contains transformed instead of Cartesian velocities. Rewritten flux vectors are as follows:

$$\hat{F}(\hat{Q}) = \sqrt{x_\eta^2 + y_\eta^2}\, T_F \bar{F} \tag{6}$$

$$\hat{G}(\hat{Q}) = \sqrt{x_\xi^2 + y_\xi^2}\, T_G \bar{G}\,, \tag{7}$$

where local rotation matrices T_F and T_G are equal to:

$$T_F = \begin{bmatrix} 1 & 0 & 0 & 0 \\ x_\tau & \hat{y}_\eta & \hat{x}_\eta & 0 \\ y_\tau & -\hat{x}_\eta & \hat{y}_\eta & 0 \\ \dfrac{x_\tau^2 + y_\tau^2}{2} & \hat{y}_\eta x_\tau - \hat{x}_\eta y_\tau & \hat{x}_\eta x_\tau + \hat{y}_\eta y_\tau & 1 \end{bmatrix}, \tag{8}$$

$$T_G = \begin{bmatrix} 1 & 0 & 0 & 0 \\ x_\tau & \hat{x}_\xi & -\hat{y}_\xi & 0 \\ y_\tau & \hat{y}_\xi & \hat{x}_\xi & 0 \\ \dfrac{x_\tau^2 + y_\tau^2}{2} & \hat{x}_\xi x_\tau + \hat{y}_\xi y_\tau & \hat{x}_\xi y_\tau - \hat{y}_\xi x_\tau & 1 \end{bmatrix}. \tag{9}$$

The modified flux vectors $\bar{F}$ and $\bar{G}$ have the following form:

$$\bar{F} = \rho \begin{bmatrix} \bar{u}_F \\ \bar{u}_F^2 + \dfrac{a^2}{\gamma} \\ \bar{u}_F \bar{v}_F \\ \bar{u}_F \bar{h}_F \end{bmatrix}, \qquad \bar{G} = \rho \begin{bmatrix} \bar{v}_G \\ \bar{u}_G \bar{v}_G \\ \bar{v}_G^2 + \dfrac{a^2}{\gamma} \\ \bar{v}_G \bar{h}_G \end{bmatrix}. \tag{10}$$

Transformed velocities in $\bar{F}$ are equal to

$$\bar{u}_F = \hat{y}_\eta (u - x_\tau) - \hat{x}_\eta (v - y_\tau) \tag{11}$$

$$\bar{v}_F = \hat{x}_\eta (u - x_\tau) + \hat{y}_\eta (v - y_\tau) \tag{12}$$

and in the $\bar{G}$ flux to

$$\bar{u}_G = \hat{x}_\xi (u - x_\tau) + \hat{y}_\xi (v - y_\tau) \tag{13}$$

$$\bar{v}_G = -\hat{y}_\xi (u - x_\tau) + \hat{x}_\xi (v - y_\tau)\,. \tag{14}$$

The terms $\hat{x}_\eta$, $\hat{y}_\eta$, $\hat{x}_\xi$, and $\hat{y}_\xi$ are normalized as follows:

$$\hat{x}_\eta = \frac{x_\eta}{\sqrt{x_\eta^2 + y_\eta^2}}, \quad \hat{y}_\eta = \frac{x_\eta}{\sqrt{x_\eta^2 + y_\eta^2}}, \quad \hat{x}_\xi = \frac{x_\xi}{\sqrt{x_\xi^2 + y_\xi^2}}, \quad \hat{y}_\xi = \frac{y_\xi}{\sqrt{x_\xi^2 + y_\xi^2}}. \tag{15}$$

The modified total enthalpies $\bar{h}_F$ and $\bar{h}_G$ have the same form as those in Cartesian components, but now with corresponding transformed velocities. a is the speed of sound and γ is the specific heat ratio. The splitting of the transformed flux vectors can now be performed in the same fashion as in Cartesian coordinates [3], but in terms of the Mach numbers $M_\xi = \bar{u}_F / a$ and $M_\eta = \bar{v}_G / a$. The flux vectors are split in such a way that the Jacobian matrices $\partial \hat{F}^+ / \partial Q$ and $\partial \hat{G}^+ / \partial Q$ have only positive eigenvalues and the Jacobian matrices $\partial \hat{F}^- / \partial Q$ and $\partial \hat{G}^- / \partial Q$ have only negative ones. Split fluxes have the form shown in equations (16).

$$\bar{F}^\pm = \begin{bmatrix} f_1^\pm = \pm \frac{\rho a}{4}\left(1 \pm M_\xi\right)^2 \\ f_2^\pm = \frac{a}{\gamma}\left[\left(\gamma - 1\right) M_\xi \pm 2\right] f_1^\pm \\ f_3^\pm = \bar{v} f_1^\pm \\ f_4^\pm = \frac{\gamma^2}{2\left(\gamma^2 - 1\right)} \frac{\left(f_2^\pm\right)^2}{f_1^\pm} + \frac{\bar{v}^2}{2} f_1^\pm \end{bmatrix}, \bar{G}^\pm = \begin{bmatrix} g_1^\pm = \pm \frac{\rho a}{4}\left(1 \pm M_\eta\right)^2 \\ g_2^\pm = \bar{u} g_1^\pm \\ g_3^\pm = \frac{a}{\gamma}\left[\left(\gamma - 1\right) M_\eta \pm 2\right] g_1^\pm \\ g_4^\pm = \frac{\gamma^2}{2\left(\gamma^2 - 1\right)} \frac{\left(g_3^\pm\right)^2}{g_1^\pm} + \frac{\bar{u}^2}{2} g_1^\pm \end{bmatrix}. \tag{16}$$

2.2. Solution method

The Euler equations in body-fitted coordinates, with flux splitting, are now given as

$$\frac{\partial \hat{Q}}{\partial \tau} + \frac{\partial \hat{F}^+}{\partial \xi} + \frac{\partial \hat{F}^-}{\partial \xi} + \frac{\partial \hat{G}^+}{\partial \eta} + \frac{\partial \hat{G}^-}{\partial \eta} = 0 \tag{17}$$

where $\hat{F}^+, \hat{F}^-, \hat{G}^+$, and $\hat{G}^-$ are split fluxes. Equation (17) is explicitly discretized and solved as shown in equation (18):

$$\begin{aligned} \hat{Q}^{n+1}(i,j) = \hat{Q}^n(i,j) - \Delta\tau \Big[& \hat{F}^+\left(i+1/2, j\right) - \hat{F}^+\left(i-1/2, j\right) + \\ & \hat{F}^-\left(i+1/2, j\right) - \hat{F}^-\left(i-1/2, j\right) + \\ & \hat{G}^+\left(i, j+1/2\right) - \hat{G}^+\left(i, j-1/2\right) + \\ & \hat{G}^-\left(i, j+1/2\right) - \hat{G}^-\left(i, j-1/2\right) \Big] \end{aligned} \tag{18}$$

where superscripts $n+1$ and n represent the new and old time steps respectively. Indices (i, j) represent the control volume centre, while $\Delta\tau$ is the time increment in the simulation. In this paper, the steady state solution is achieved by the time marching calculations. The difference between two neighbouring grid lines in body-fitted coordinates is taken to be unity. The spatial derivatives are approximated by MUSCL differencing, where fluxes are calculated indirectly by extrapolating the solution vector by backward or forward formulas depending on which flux is concerned. General formulas for calculating split fluxes are as follows:

$$\hat{F}^{\pm}(i-1/2,j)=\hat{F}^{\pm}\left(Q^{\mp}_{i-\frac{1}{2},j},m_{i-\frac{1}{2},j}\right),\quad \hat{F}^{\pm}(i+1/2,j)=\hat{F}^{\pm}\left(Q^{\mp}_{i+\frac{1}{2},j},m_{i+\frac{1}{2},j}\right) \tag{19}$$

$$\hat{G}^{\pm}(i,j-1/2)=\hat{G}^{\pm}\left(Q^{\mp}_{i,j-\frac{1}{2}},m_{i,j-\frac{1}{2}}\right),\quad \hat{G}^{\pm}(i,j+1/2)=\hat{G}^{\pm}\left(Q^{\mp}_{i,j+\frac{1}{2}},m_{i,j+\frac{1}{2}}\right). \tag{20}$$

The term m represents all geometric terms involved in the transformation to the body-fitted coordinates. Indices $i-1/2$, $i+1/2$, $j-1/2$, and $j+1/2$ represent the values at control volume faces as shown in Fig. 1. The extrapolated values of the solution vector Q are determined with second order accuracy formulas:

$$Q^{-}_{i+\frac{1}{2},j}=Q_{i,j}+0.5\left(Q_{i,j}-Q_{i-1,j}\right) \tag{21}$$

$$Q^{+}_{i+\frac{1}{2},j}=Q_{i+1,j}+0.5\left(Q_{i+1,j}-Q_{i+2,j}\right). \tag{22}$$

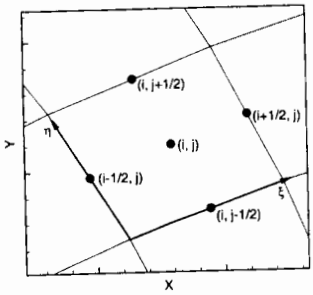

Fig. 1 Control volume indices

2.3. Boundary conditions

The boundary condition on the airfoil is imposed by setting the normal relative velocity to zero:

$$\left(\vec{v}-\vec{v}_b-\vec{v}_t\right)\cdot\vec{n}=0, \tag{23}$$

where $\vec{v}$, $\vec{v}_b$, and $\vec{v}_t$ are fluid velocity, prescribed velocity of airfoil contour, and transpiration velocity, respectively. The transpiration velocity represents the boundary layer effect of growing displacement thickness. This is the way the boundary layer model is coupled to the inviscid model. The pressure is determined from the normal component of the momentum equation, which is derived by applying the total derivative with respect to time to equation (23):

$$\frac{D\vec{v}}{Dt}\cdot\vec{n}-\frac{D\left(\vec{v}_b+\vec{v}_t\right)}{Dt}\cdot\vec{n}+\left(\vec{v}-\vec{v}_b-\vec{v}_t\right)\cdot\frac{D\vec{n}}{Dt}=0. \tag{24}$$

The first member in equation (24) represents the left hand side of momentum equation in the direction of the unit normal $\vec{n}$. When this is taken into account, then the following equation is derived:

$$\rho\left\{\frac{D\vec{n}}{Dt}\cdot\left(\vec{v}-\vec{v}_b-\vec{v}_t\right)-\frac{D\left(\vec{v}_b+\vec{v}_t\right)}{Dt}\cdot\vec{n}\right\}=grad\,p\cdot\vec{n} \tag{25}$$

where D/Dt is the total derivative with respect to the physical time. On the far field of computational domain, the characteristic boundary condition is used. The problem is locally regarded as one-dimensional, i.e. derivatives along the boundary $\partial(\ )/\partial\xi\to 0$ can be neglected and, according to Thomas [4], the characteristic equations can be constructed and from them the Riemann invariants can be derived:

$$R^{\pm}=v_n\pm\frac{2a}{\gamma-1}, \tag{26}$$

where a is the local speed of sound and v_n is the local velocity perpendicular to the far-field boundary. The characteristic equations are used to update the variables on the boundary at a new time level. For a two-dimensional case, four primitive variables will be needed and consequently four independent equations are needed. For the subsonic inlet far-field boundary condition, where $v_n<0$, the following expressions are valid:

$$R^{+}=R^{+}(\infty),\qquad R^{-}=R^{-}(F),\qquad v_t=v_t(\infty),\qquad p_T=p_T(\infty). \tag{27}$$

For the subsonic outflow far-field boundary condition, where $v_n>0$, the following equations are valid:

$$R^{+}=R^{+}(F),\qquad R^{-}=R^{-}(\infty),\qquad v_t=v_t(F),\qquad p_T=p_T(F). \tag{28}$$

The symbol F denotes that characteristic variables are extrapolated locally from interior field values, and the symbol ∞ denotes that variables are calculated from the far-field representation. p_T in equations (27) and (28) is the total pressure.

2.4. Viscous model

The method decouples the inviscid region surrounding the airfoil from the thin viscous region close to the airfoil. The viscous region is evaluated according to Drela's method of integral boundary layer equations [5], which are the integral momentum equation

$$\frac{d\theta}{d\xi}=\frac{C_f}{2}-\left(H+2-M_e^2\right)\frac{\theta}{u_e}\frac{du_e}{d\xi} \tag{29}$$

and the integral kinetic energy equation, also known as the shape parameter equation,

$$\frac{dH^*}{d\xi}=\frac{2C_D}{\theta}-\frac{H^*}{\theta}\frac{C_f}{2}-\left(\frac{2H^{**}}{H^*}+1-H\right)\frac{H^*}{u_e}\frac{du_e}{d\xi}, \tag{30}$$

where θ is the momentum thickness, C_f the friction coefficient, H the shape parameter, M_e the Mach number at the boundary layer edge, u_e the velocity at the boundary layer edge, s is the coordinate originating at the stagnation point and going over the upper and the lower airfoil contour toward the trailing edge, H^* the kinetic energy shape parameter, C_D the dissipation coefficient, and H^{**} is the density shape parameter. The subscript e in equations (29), (30) and all subsequent equations represents variable values for the boundary layer edge. The momentum and shape parameter equations are valid for both laminar and turbulent boundary layers. These equations contain more than two dependent variables and hence some assumptions about the additional unknowns will have to be made. If two variables, θ and δ^*,

are defined, then four additional closure equations are needed. Additional closure equations are given in [6]. The computational grid for boundary layer calculations was one dimensional with the same number of main nodes as the number of control volumes surrounding the airfoil contour.

The method for determining the onset of transition is derived from the theory of spatial amplification based on the Orr-Sommerfeld equation [7]. This method is also known as the e^n method. The growth in disturbances is responsible for the onset of the transition in the boundary layers. The method determines the amplitude of the disturbances by the integration of disturbance growth rate from the point of instability. The transition occurs when the amplitude grows by more than a factor $e^n = e^9$. The exponent n can be different from 9; actually, it can vary between 7 and 11 depending mainly on the free stream turbulence and the surface roughness [8].

2.5. Viscous-inviscid coupling

The viscous-inviscid coupling between the boundary layer and the Euler equations is made by the transpiration velocity concept or equivalent sources concept as proposed by Lighthill [9]. The transpiration velocity changes the slope of the net velocity at the boundary and thus represents the displacement thickness of boundary layer and the influence of the boundary layer on the inviscid flow outside the boundary layer. The transpiration velocity is defined as

$$v_t = \frac{d}{ds}\left(u_e \delta^*\right). \tag{31}$$

In this study, viscous-inviscid coupling is made in a direct mode. The scheme of direct mode coupling is shown in Fig. 2. In such an approach, the output from the inviscid solver, which is the velocity or the pressure at the boundary layer edge, is used as the input for the viscous solver of boundary layer equations. The output from the viscous solver is the displacement thickness, or the transpiration velocity derived from the displacement thickness, which is then used as the input for the inviscid solver to update the boundary condition at the airfoil contour. The advantage of such coupling method is its speed and simplicity in application. The disadvantage of the direct coupling is the inability to simulate separated flows because of the appearance of a singularity in the boundary layer equations called Goldstein's singularity [10]. The coupling method used in this study showed strong solution oscillation in the near separation test cases and at the

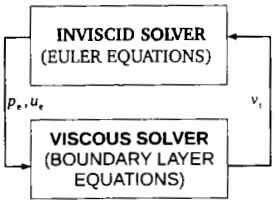

Fig. 2 The direct method scheme of viscous-inviscid coupling

position of sudden thickening of the boundary layer. To reduce such oscillatory behaviour of the solution and to reach a monotone converged solution, the under-relaxation method was employed. The under-relaxation is performed on the transpiration velocity by the following expression:

$$v_t = v_t^o + \beta\left(v_t^n - v_t^o\right) \tag{32}$$

The superscripts o and n represent the old and the new solution of transpiration velocity magnitude in two successive iterations respectively. β represents the under-relaxation factor and its value is smaller than one. In the near separation test cases, which are the most difficult cases for such methods, the under-relaxation factor adopts very small values around 0.001. This is the most critical part of the method. At the initial calculation step when the transpiration velocity magnitude is calculated for the first time, its old value is equal to zero. The left hand side of equation (32) is a resulting transpiration velocity magnitude and it serves as the old solution in the subsequent iteration.

3. Results and discussion

The results for five steady test cases with and without the appearance of a shock wave are shown. First two test cases are calculated with the NAC0012 airfoil, the third with the NACA64A010 airfoil and the last two with the NLR 7301 supercritical airfoil. These airfoils show three different characteristic pressure distributions. The calculated results for the viscous-inviscid interaction method are compared with the test cases from AGARD reports [11], [12] and with the RANS code Tau [13] for the NACA0012 airfoil only. For other two airfoils, the viscous-inviscid results were compared with experimental data only. All calculations in the Tau code were performed with the two-equation k-ω based turbulence model LEA (Linearized Explicit Algebraic stress model) which is derived by Rung from the RQEVM (Realizable Quadratic Explicit Algebraic Stress Model) [14]. The flow was treated as completely turbulent without limiting the production of turbulence in the laminar part of the boundary layer.

3.1. NACA0012 results

In Table 1 the selected test cases for the NACA0012 airfoil from experimental data in the AGARD report [11] are presented. Two test cases at different Mach numbers, which cover the subsonic compressible flow with the occurrence of a shock wave, are selected.

Table 1 NACA0012 steady test cases

Test case	*Ma*	*Re*	α
1	0.756	$4.01 \cdot 10^6$	$-0.01°$
2	0.803	$4.09 \cdot 10^6$	$0.05°$

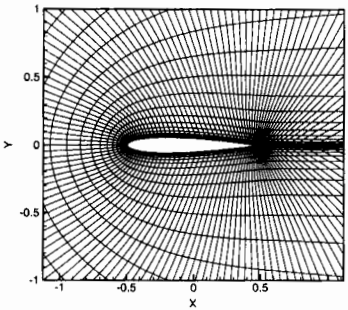

Fig. 3 Computational grid around NACA0012 airfoil

The C-type computational grid for the NACA0012 airfoil test case is shown in Fig. 3. It is a structured grid generated by the elliptic grid generator. In Fig. 4, the calculated steady pressure coefficient results for test case 1 are presented and compared with experimental data

and the RANS results for the upper (left side of the figure) and the lower (right side of the figure) airfoil contour. The calculated results show good agreement with experimental data. Two little jumps in the pressure coefficient on the upper and the lower side for the viscous-inviscid results and the experimental data can be observed. The first jump is because of a weak shock wave and the second one because of the existence of transition region in the boundary layer. The transition region jump is indicated in the figure. Small deviations of RANS results compared to experimental data can be observed at the weak shock wave position, while the viscous-inviscid method gives good results in this position.

Small deviations of RANS results compared to experimental data can be observed at the weak shock wave position, while the viscous-inviscid method gives good results in this position. The viscous-inviscid method shows small deviations at the trailing edge of the airfoil. It is shown that the transition method e^n (where $n=9$) accurately estimates the transition region of the boundary layer. From the pressure coefficient distribution it seems that the RANS results calculated with the turbulent flow for the whole region give a too strong shock wave with respect to the experimental data. The reason for

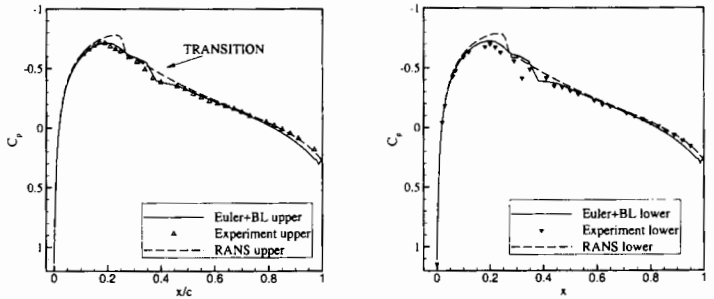

Fig. 4 NACA0012 steady pressure coefficient distribution for upper (left) and lower (right) airfoil contour for test case 1, $Ma=0.756$, $Re=4.01\cdot10^6$, $\alpha=-0.01°$

this can be in the steeper growth in displacement thickness in the turbulent boundary layer than in the laminar boundary layer. This leads to compression in the outer inviscid flow which causes the shock wave to appear at smaller angles of attack.

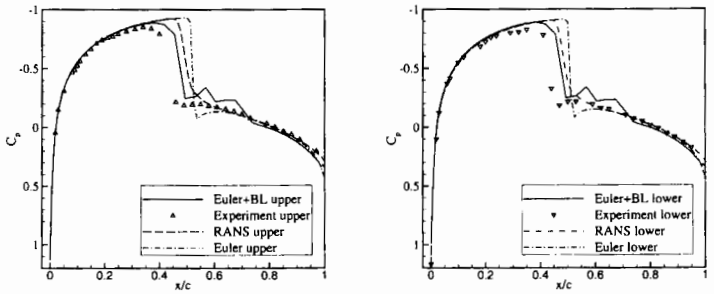

Fig. 5 NACA0012 steady pressure coefficient distribution for the upper (left) and the lower (right) airfoil contour for test case 2, $Ma=0.803$, $Re=4.09\cdot10^6$, $\alpha=0.05°$

In Fig. 5, the NACA0012 steady state calculated results and the experimental data on the upper (left side of the figure) and the lower (right side of the figure) airfoil contour are presented for test case 2. This test case represents the flow with a strong shock wave. The calculated results and experimental data show the existence of strong shock wave at the position of 45% of the airfoil chord length from the leading edge, which is in good agreement with experimental data.

Viscous effects move the shock wave position toward the airfoil leading edge, which can be seen in Fig. 5 where the solution for inviscid flow (Euler solution) is also given.

The results for the inviscid flow give the shock wave position moved toward the trailing edge with respect to the viscous flow solutions. This test case and similar test cases, where a strong shock wave appears, represent a difficult task for the viscous-inviscid interaction method presented in this article. This difficulty appears as a slow convergence rate and non-monotone convergence. To stabilize the convergence, under-relaxation is employed. A possible reason for instability is the boundary layer coupling by transpiration velocity and the direct solution method of boundary layer equations. Test case 2 is close to the separation bubble occurrence where the direct solution method of boundary layer equations is singular.

3.2. NACA64A010 results

A test case for the NACA64A010 airfoil is selected from the AGARD report [12]. Flow conditions are presented in Table 2.

Table 2 NACA64A010 steady test case

Test case	*Ma*	*Re*	α
3	0.796	$12.56 \cdot 10^6$	-0.21°

For the Euler solution, the structured C-type grid which consisted of 9600 control volumes was used. A close view of the grid around the NACA64A010 airfoil is shown in Fig. 6.

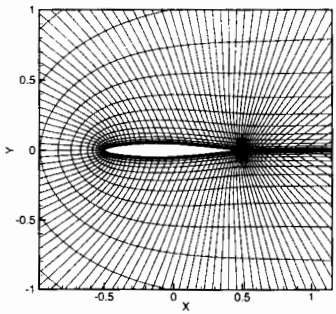

Fig. 6 Computational grid around the NACA64A010 airfoil

The calculated viscous-inviscid interaction method results for the NACA64A010 test case are compared with experimental data from the AGARD report [12] and are shown in Fig. 7. This test case has a flow field that contains a supersonic region with a weak shock wave. The calculated results for the upper airfoil contour show good agreement, except at the position of the shock wave in which the pressure peak is under-predicted. At the shock wave position for the upper and also for the lower airfoil contour, the calculated results show the smoothing of pressure jump with respect to experimental data. This could indicate too strong impact of the boundary layer on the shock wave intensity. Due to the boundary layer thickening in the foot

of the shock wave, a lambda shaped compression shock appears. As a consequence, the shock wave intensity is smoothed and this can be seen in the pressure coefficient distribution on the airfoil contour [15], [16]. On the front part of the lower surface, the numerical solution shows a noticeable deviation from experimental data.

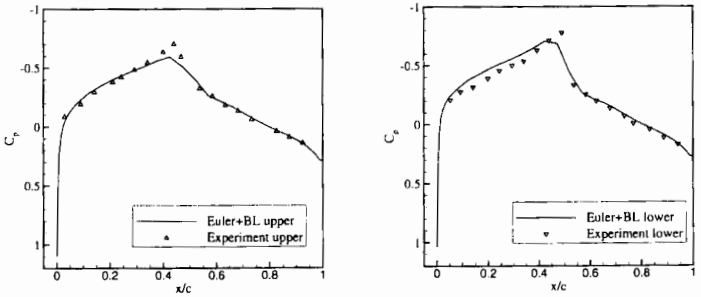

Fig. 7 NACA64A010 steady pressure coefficient distribution for the upper (left) and the lower (right) airfoil contour at $Ma=0.796$, $Re=12.56\cdot 10^6$, $\alpha=-0.21°$

3.3. NLR7301 results

The NLR7301 airfoil is among the thickest supercritical airfoils with a value of 16.5% relative thickness (relative to chord length). Because of rather extreme nose radius this airfoil represents a hard test case for viscous-inviscid interaction methods. Compared to conventional airfoils, the NLR7301 airfoil has a reduced amount of camber, an increased leading edge radius, small surface curvature on the suction side and concavity in the rear part of the overpressure side. In the design flow conditions, this and similar supercritical airfoils typically develop a larger supersonic region, closed by a weak shock wave or, in an ideal case, a shock-free recompression which leads to a smaller drag coefficient and larger rear loading [17]. In off-conditions, an increase in the Mach number or in the angle of attack leads to the increase in the shock strength and in the subsequent thickening of the boundary layer. This could result in the shock induced boundary layer separation behind the shock and ultimately in a complete separation from the shock position to the trailing edge. Such flow conditions are very unfavourable for viscous-inviscid interaction methods and therefore for the one used in this investigation.

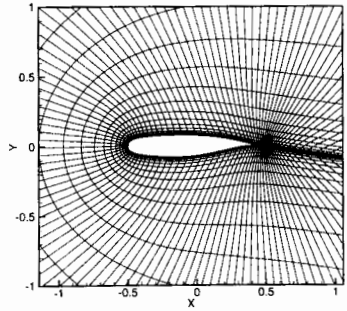

Fig. 8 Computational grid around NLR7301 airfoil

A C-type structured computational grid which contained 9600 control volumes was used. The computational grid around the NLR7301 airfoil is shown in Fig. 8. Two test cases for the NLR7301 airfoil were performed as presented in Table 3.

Table 3 NLR7301 steady test cases

Test case	*Ma*	*Re*	α
4	0.299	$1.1 \cdot 10^6$	0.3966°
5	0.599	$1.9 \cdot 10^6$	0.3832°

Fig. 9 presents the results calculated by the viscous-inviscid interaction method and the experimental data for the two test cases. The calculated results show moderate agreement with the experimental data in the whole region except at the upper airfoil contour near the trailing edge and at the transition region where bigger deviations are present. Such disagreement is probably caused by the violation of boundary layer assumptions. The NLR 7301 airfoil has a leading edge part with a very small radius which violates the assumptions made in the derivation of boundary layer equations. The second cause of such disagreement on the upper side toward the trailing edge could be in the rear type separation on such an airfoil described before. In such a case, the boundary layer thickness violates the assumptions made in the derivation of boundary layer equations. Such rear-loaded airfoils have low upper-pressure up to a high percentage of the chord, followed by a strong adverse pressure gradient, which causes a rapid boundary-layer growth. This kind of airfoil flow is very sensitive to any disturbance from the wall boundary, which means also from the boundary layer. Altogether, the presented viscous-inviscid method gives results with moderate agreement on this kind of airfoils and also shows very non-monotone convergence and a long time convergence history. The under-relaxation factor employed in the calculation of test cases 4 and 5 was is equal to $\beta = 0.001$.

The viscous-inviscid calculation started after reaching a steady inviscid solution of constant normal force coefficient. The convergence criterion was reached when pressure residual decreased to 10^{-3}. The pressure residual was calculated for all points on the airfoil contour as follows:

$$\text{res}_p = \frac{p^n - p^o}{p^o}. \tag{33}$$

The indices o and n represent the old and new time steps. The convergence criterion was reached when the criterion is satisfied at all the points.

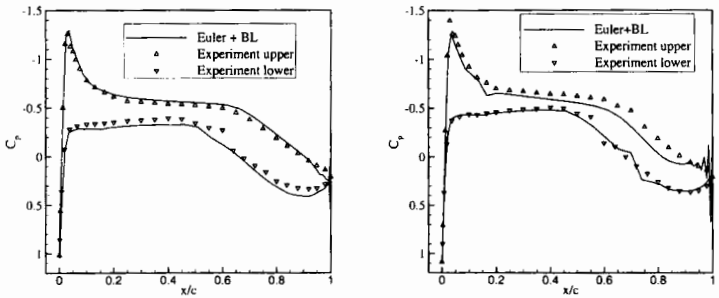

Fig. 9 NLR7301 steady pressure coefficient distribution for test case 4 (left) and test case 5 (right)

At the trailing edge, the method shows pressure oscillations on the upper airfoil contour where the turbulent boundary layer is extremely thick. This could be explained by the separation of type B described in [18]. The reason for such separation lies in a steep pressure gradient towards the trailing edge and this type of separation starts from the trailing edge (rear separation). The rear separation depends strongly on the boundary layer thickness, the velocity profile of the boundary layer approaching the trailing edge, and on the pressure gradient. Therefore, the B-type separation is very sensitive to the location of the point where transition takes place. Also, the reason for pressure oscillations at the trailing edge could be in the violation of normal boundary layer assumption ($\partial p/\partial n=0$) at the trailing edge, namely the pressure gradient perpendicular to the boundary layer direction near the trailing edge can be significant.

4. Conclusion

In this study, a simple and accurate method for steady aerodynamic load prediction is developed. The steady test cases were performed for the NACA0012, NACA64A010, and NLR7301 airfoils. The test cases for the NACA0012 and NACA64A010 airfoils were run for a transonic flow with the occurrence of a shock wave, while the NLR7301 cases were run for a subsonic flow and a transonic flow without the occurrence of shock waves. All test cases were run in the range of angles of attack where no massive flow separation is expected. The obtained results are compared with experimental data and with the calculated results of steady RANS code.

The calculated steady results for the NACA0012 and NACA64A010 airfoils show good agreement with the experimental data at all Mach numbers.

For these two airfoils, the position of transition is accurately predicted. In the case without shock, the transition is indicated as a small jump in the distribution of the pressure coefficient, as in the experimental data. In the cases with a shock wave, transition occurs at the shock position, so it is not clearly evident.

For the two airfoils, the strength of shock wave is well predicted but its position is slightly moved toward the trailing edge with respect to the experimental data. The developed method predicts the shock wave position closer to the experimental one than the pure inviscid method, which means that accounting for the boundary layer effects improves the result accuracy.

The results for the NLR7301 airfoil (which represents a challenge for viscous-inviscid methods because of extremely big nose radius) show strong sensitivity to the boundary layer thickening and the position of transition point. The developed method for this airfoil shows results with moderate agreement in pressure distribution prediction. Also, the predicted transition point on the compression side of the airfoil is not positioned in the right place and the method shows pressure instabilities at the suction side of the trailing edge.

It can be concluded that the inclusion of boundary layer into the steady Euler method results in a more accurate prediction method for steady aerodynamic loads. The developed method is fast and gives results of nearly the same accuracy as a higher mathematical model like RANS and of good agreement with experimental data.

REFERENCES

[1] Leifsson, L., Koziel, S.: Multi-fidelity design optimization of transonic airfoils using physics-based surrogate modelling and shape-preserving response prediction, Journal of Computational Science, Vol. 1, No. 2, 2010., p. 98-106

[2] Hacioglu, A., Özkol, I.: Transonic Airfoil Design and Optimisation by Using Vibrational Genetic Algorithm, Aircraft Engineering and Aerospace Technology, Vol. 75, No. 4, 2003.

[3] Anderson, W.K., Thomas, J.L., Van Leer, B.: Comparison of Finite Volume Flux Vector Splittings for the Euler Equations, AIAA Journal, Vol. 24, No. 9, 1986., 1453 – 1460

[4] Thomas, J.L., Salas, M.D.: Far-Field Boundary Condition for Transonic Lifting Solutions to the Euler Equations, AIAA Journal, Vol. 24, No. 7, 1986., 1074-1080

[5] Drela, M., Giles, M.B.: Viscous-Inviscid Analysis of Transonic and Low Reynolds Number Airfoils, AIAA Journal, Vol. 25, No. 10, 1987., 1347-1355

[6] Majić, F.: Boundary Layer Method for Unsteady Aerodynamic Loads Determination, doctoral thesis, Universitiy of Zagreb, Zagreb, 2010.

[7] Obremski, H.J., Morovkin, M.V., Landahl, M.T.: A Portfolio of Stability Characteristics of Incompressible Boundary Layer, AGARD-ograph 134, NATO, Neuilly Sur Seine, France, 1969.

[8] Drela, M.: Two-Dimensional Transonic Aerodynamic Design and Analysis Using the Euler Equations, Ph.D. thesis, Massachusetts Institute of Technology, 1986.

[9] Lighthill, M.J.: On Displacement Thickness, Journal of Fluid Mechanics, Vol. 4, No. 4, 1958., 383-392

[10] Goldstein, S.: On Laminar Boundary-Layer Flow Near a Position of Separation, Quarterly Journal of Mechanics and Applied Mathematics, No. 1, 1948., 43-69

[11] Thibert, J.J., Grandjacques, M., Zwaaneveld, J.: Experimental Data Base for Computer Program Assessment – Report of the Fluid Dynamics Panel Working Group 04, AGARD-AR 138, 1979.

[12] Landon, R.H., Davis, S.S.: Compendium of Unsteady Aerodynamic Measurement, AGARD-R 702, August 1982.

[13] Deutsches Zentrum für Luft- und Raumfahrt: Technical Documentation of the DLR TAU-Code

[14] Rung, T., Lübcke, H., Franke, M., Xue, L., Thiele, F., Fu, S.: Assessment of Explicit Algebraic Stress Models in Transonic Flows, Engineering Turbulence Modelling and Experiments 4, Proc. 4th Int. Symposium on Engineering Turbulence Modelling and Measurements, Corsica, France, Elsevier, Amsterdam, 1999., 659-668

[15] Magnus, R., Yoshihara, H.: Inviscid Transonic Flow Over Airfoils, AIAA Journal, Vol. 8, No.12, 1970., 2157-2161

[16] Anderson, J.D.Jr.: Modern Compressible Flow, McGraw-Hill Publishing Company, 1990.

[17] Soda, A.: Numerical Investigation of Unsteady Transonic Shock/Boundary Layer Interaction for Aeronautical Applications, Forschungsbericht 2007-03, Deutsches Zentrum für Luft- und Raumfahrt, March 2007.

[18] Tijdeman, H.: Investigation of the Transonic Flow Around Oscillating Airfoils, NLR TR 77090 U, October 1977.

Submitted: 08.3.2011

Accepted: 03.6.2011

Dr. sc. Frane Majić
Prof. dr. sc. Zdravko Virag
Faculty of Mechanical Engineering and Naval Architecture, Ivana Lučića 5, 10000 Zagreb, Croatia